

Triggering global climate transitions through volcanic eruptions

Article

Accepted Version

Gupta, M., Marshall, J. and Ferreira, D. ORCID:
<https://orcid.org/0000-0003-3243-9774> (2019) Triggering global climate transitions through volcanic eruptions. *Journal of Climate*, 32 (12). pp. 3727-3742. ISSN 1520-0442 doi:
<https://doi.org/10.1175/JCLI-D-18-0883.1> Available at
<https://centaur.reading.ac.uk/83783/>

It is advisable to refer to the publisher's version if you intend to cite from the work. See [Guidance on citing](#).

To link to this article DOI: <http://dx.doi.org/10.1175/JCLI-D-18-0883.1>

Publisher: American Meteorological Society

All outputs in CentAUR are protected by Intellectual Property Rights law, including copyright law. Copyright and IPR is retained by the creators or other copyright holders. Terms and conditions for use of this material are defined in the [End User Agreement](#).

www.reading.ac.uk/centaur

CentAUR

Central Archive at the University of Reading

Reading's research outputs online



Triggering global climate transitions through volcanic eruptions

Mukund Gupta ^{*}, John Marshall [†], David Ferreira [‡]

Massachusetts Institute of Technology, Cambridge, MA/USA

⁴ **Corresponding author address:* Mukund Gupta, Department of Earth, Atmosphere and Planetary
⁵ Sciences, Massachusetts Institute of Technology, 77 Massachusetts Avenue, Cambridge, MA/USA
⁶ E-mail: guptam@mit.edu

⁷ [†]Department of Earth, Atmosphere and Planetary Sciences, Massachusetts Institute of Technology,
⁸ 77 Massachusetts Avenue, Cambridge, MA/USA

⁹ [‡]Department of Meteorology, University of Reading, Reading, UK

ABSTRACT

10 A coupled climate model with idealized representations of atmosphere,
11 ocean, sea ice and land is used to investigate transitions between global cli-
12 mate equilibria. The model supports the presence of climates with limited ice
13 cover (Warm), a continuum of climates in which sea ice extends down into the
14 mid-latitudes and the tropics (Cold), together with a completely ice-covered
15 earth (Snowball). Transitions between these states are triggered through vol-
16 canic eruptions, where the radiative effect of stratospheric sulfur emissions is
17 idealized as a 1-year impulse reduction in incoming solar radiation. Snow-
18 ball transitions starting from the Cold state are more favorable than from the
19 Warm state, because less energy must be extracted from the system. However,
20 even when starting from a Cold climate, Toba-like volcanic events (cooling
21 of order -100 Wm^{-2}) must be sustained continuously for several decades to
22 glaciare the entire planet. When the deep ocean is involved, the volcanic re-
23 sponse is characterized by relaxation timescales spanning hundreds to thou-
24 sands of years. If the interval between successive eruptions is significantly
25 shorter (years to decades) than the ocean's characteristic timescales, the cu-
26 mulative cooling can build over time and initiate a state transition. The model
27 exhibits a hysteresis loop in which the Cold equilibrium branch is not directly
28 accessible from the Snowball state, but when starting from a Cold climate, the
29 system can transition back to an ice-free state without hysteresis.

30 **1. Introduction**

31 Paleoclimate reconstructions have shown that Earth has experienced a wide array of climates
32 over the last billion years. At its most extreme, the climate has ranged between hothouse worlds
33 with little or no ice at the poles and deep ocean temperatures upwards of 20°C (e.g. Tripathi and
34 Elderfield (2005)), to Snowball periods in which ice covered most of the Earth's surface (e.g.
35 Hoffman et al. (1998)). The ability of the climate to exist in a number of dynamical states was
36 discussed by Stommel (1961) with regards to the bi-stability of the oceanic meridional overturning
37 circulation (MOC). This work suggested that the MOC could exhibit two stable states, namely a
38 vigorous circulation mode driven by temperature and a weak mode controlled by salinity. Another
39 source of instability in the climate is the ice-albedo feedback, which was first investigated by
40 Budyko (1969) and Sellers (1969) in simple energy balance models (EBMs). These studies found
41 that the Earth could exist in a stable state with either a small amount of ice at the poles or with
42 complete ice cover. Rose and Marshall (2009) modified the EBM to demonstrate that an additional
43 state with a large ice cap can be stabilized by the meridional convergence of heat transported by
44 the ocean subtropical cells. Indeed several General Circulation Models (GCMs) have shown that
45 climates with ice extending down to the mid-latitudes or the tropics are realizable when ocean heat
46 transport (OHT) can arrest the advance of sea ice at those latitudes (e.g. Poulsen and Jacob (2004),
47 Langen (2004), Ferreira et al. (2011) and Rose et al. (2013)) or when the meridional gradient in
48 ice albedo can limit the strength of the positive ice-albedo feedback (Abbot et al. (2011)).

49 Transitions between these multiple equilibria require global-scale forcings that push the climate
50 away from its original equilibrium to the next stable state. Many of the long-lasting climatic
51 shifts that occurred in the last billion years were governed by the balance between weathering
52 of silicate rocks and the input of carbon dioxide by volcanic eruptions in the atmosphere, which

53 typically spans 10^5 - 10^6 year timescales (Walker et al. (1981)). However, large perturbations in
54 the atmosphere's radiation budget acting over much shorter (\sim decadal) timescales could have also
55 caused severe episodes of climate change. Perhaps one of the largest forcings ever experienced
56 by the Earth's climate was the Chicxulub asteroid impact 66 millions years ago, during which
57 the amount of dust and sulfate aerosols in the atmosphere could have blocked more than half of
58 the solar radiation reaching the Earth's surface for several years, subsequently leading to extreme
59 cooling and the beginning of a mass extinction (Brugger et al. (2017), Kaiho and Oshima (2017)).

60 The volcanic emission of sulfur particles into the stratosphere is also known to cool the sur-
61 face of the Earth for several years after the eruption (Robock (2000)). Over the last few thousand
62 years, these volcanic forcings were too weak and short-lived to have caused a drastic shift in cli-
63 matic state. However, there have been recorded instances of volcanic activity much larger than
64 that of the Holocene, which may have triggered a significant glaciation (e.g. Rampino and Self
65 (1992), Prueher and Rea (2001)). The Toba super-eruption around 73.5 ka before present had a
66 sulfur loading that was two orders of magnitude larger than the 1991 Mt Pinatubo eruption, and
67 could have reduced incoming solar radiation by a third for several years after the event (Timm-
68 reck et al. (2010)). While GCM simulations with these types of forcings did not yield widespread
69 glaciation (Jones et al. (2005)), some authors have argued that a sequence of super-eruptions sep-
70 arated by a short time interval could eject enough sulfur particles into the stratosphere to trigger
71 a significant shift in Earth's history, such as a mass extinction (Baresel et al. (2017)) or a Snow-
72 ball Earth (Stern et al. (2008), Macdonald and Wordsworth (2017)). In particular, Macdonald and
73 Wordsworth (2017) argue that starting from the cool Neoproterozoic background climate, a suc-
74 cession of super-eruptions occurring over several decades could have initiated the Snowball event
75 of the Sturtian (717 - 616 Ma). While this estimate was obtained using a single-column climate

76 model with a heat capacity corresponding to the mixed layer depth of the ocean (~ 50 m), Voigt
77 and Marotzke (2010) and Voigt et al. (2011) argue that the entire ocean must cool to the freezing
78 point to initiate a Snowball climate. In the present study, we explore the extent to which the ocean
79 constrains the forcing magnitude and timescale required for global climate transitions using a cou-
80 pled Atmosphere-Ocean-Ice GCM (which we refer to here as the ‘climate model’), and explore
81 whether volcanic eruptions could successfully initiate a drastic climatic state change, such as a
82 Snowball transition.

83 The presence of multiple equilibria in the global climate can also affect the transition behavior
84 of the system. While Voigt and Marotzke (2010) did not find intermediate stable states between
85 their reference ‘warm’ climate and the Snowball, the following work of Voigt et al. (2011), Voigt
86 and Abbot (2012), Yang et al. (2012), and others did find such states. The GCM used in this study
87 allows the existence of a continuum of climates with sea ice extending from the mid-latitudes to
88 the tropics (45° to 25° latitude), owing to the stabilizing nature of meridional heat transport by
89 subtropical oceanic cells (e.g. Rose and Marshall (2009), Ferreira et al. (2011)). We initiate tran-
90 sitions starting from these different states and evaluate how the proximity to a transition threshold
91 affects the timescale required to tip the climate to a new state. Moreover, a number of studies have
92 suggested that a Waterbelt (or Slushball) climate with ice extending down to the tropics could
93 better explain the survival of oceanic life during the Sturtian (717 - 616 Ma) and Marinoan (650 -
94 635 Ma) glaciations events, as opposed to a complete Snowball (e.g. Hoffman et al. (2017)). The
95 climate model used in this study shows that a Waterbelt-like climate may occur for a significantly
96 smaller threshold forcing than that required for complete glaciation, but unlike the Snowball, this
97 state exhibits no hysteresis when the forcing is removed.

98 Our paper is set out as follows: Section 2 introduces the coupled climate model; Section 3
99 presents its equilibrium states. Section 4 focuses on the transition behavior, first from step and
100 then from impulse volcanic forcings. Section 5 concludes.

101 **2. The coupled climate model and modeling framework**

102 Numerical experiments are carried out with the coupled atmosphere, ocean, sea ice and land
103 model based on the MITgcm (Marshall et al. (1997a), Marshall et al. (1997b)). The particular
104 setup of the model used here comprises a 'boomerang' configuration, which consists of two 45°
105 wide flat continents separated by a 90° angle such that the ocean is split into a narrow Atlantic-
106 like basin and a wide Pacific-like basin connected to an unblocked 'Southern Ocean' in the South
107 (see Ferreira et al. (2018)). The ocean is flat-bottomed with a uniform depth of 3000 m. The
108 atmospheric scheme is based on the simplified parameterizations of primitive-equation dynamics
109 (SPEEDY) from Molteni (2003) at five level vertical resolution. It includes a four-band radiation
110 scheme, a parameterization of moist convection, diagnostic clouds and a boundary layer scheme.
111 In the reference states, the solar constant (divided by 4) is 341.5 Wm^{-2} . Despite the idealized
112 nature of the model, it captures many of the essential large-scale features of the climate such as an
113 overturning circulation dominated by the small basin, atmospheric storm tracks and hydrological
114 cycle, gyres and a circumpolar current in the oceans, and a seasonal sea ice cycle. Additional
115 modelling details are provided in the Supplementary Information (SI).

116 Perturbation experiments are conducted by reducing the TOA insolation. The forcing F is di-
117 agnosed as the net radiative imbalance at the TOA, averaged over the first year of the simulation.
118 For step forcing experiments, the insolation is changed abruptly at $t = 0$ and subsequently held
119 constant in time. For volcanic forcing experiments, we crudely emulate the effects of stratospheric

120 aerosol injection by uniformly reducing the insolation for one year and subsequently turning the
121 forcing off (as in Gupta and Marshall (2018)). We also conduct simulations comprising successive
122 eruptions separated by a specified time interval.

123 **3. Stable climate states of a coupled climate model**

124 *a. Equilibrium solutions*

125 Figure 1 shows the three equilibrium branches found in our model: Warm, Cold and Snowball.
126 Note that we reserve the term 'state' for individual points on a given equilibrium branch. The
127 Warm reference state has some sea ice in the Southern hemisphere (SH) but none in the Northern
128 hemisphere (NH). It has a globally-averaged ocean potential temperature $\theta = 8.3$ °C and a global
129 mean sea surface temperature (SST) of 19.6 °C. The Cold equilibrium consists of a continuum of
130 states with sea ice latitude ranging from 45° to 25° and θ between 0.5 and -1.7 °C. The mildest
131 states on this Cold branch have an ice cap extending down to the mid-latitudes, which is remi-
132 niscent of the glacial climate of the Pleistocene (Ferreira et al. (2018)). The most extreme states
133 on the Cold branch have sea ice reaching down to the tropics, which is analogous to Waterbelt or
134 Slushball states found by other studies (e.g. Rose (2015) and Abbot et al. (2011)). Since these
135 Waterbelt-like climates are plausible analogs for the state of the Earth during the Neoproterozoic
136 glaciations, it is instructive to treat them somewhat separately than the rest of the Cold branch,
137 particularly in the context of state transitions. In what follows, we thus choose to refer to Cold
138 states with $\theta < -1.5$ °C as Waterbelts, and others simply as Cold. Our discussion does not depend
139 strongly on this threshold, as long as it is chosen close enough to the freezing point. Finally, the
140 Snowball is fully ice covered with $\theta = -1.8$ °C (the mean freezing point of the ocean). Simulations

141 that reach this state are stopped when the whole ocean reaches the freezing temperature, to avoid
142 runaway ice growth in the absence of geothermal heat flux.

143 Figure 1 also presents the various equilibrium states in terms of their energy levels E , approx-
144 imated by the sum of ocean heat content and latent energy stored in the sea ice, all measured
145 relative to the Warm state.

$$E = \rho c H_{tot} (\theta - \theta_w) + A^{-1} L_f (M - M_w) \approx \rho c H_{tot} (\theta - \theta_w), \quad (1)$$

146 where ρ is the sea water density, c is the thermal heat capacity of water, H_{tot} is the globally area-
147 averaged ocean depth, θ is the ocean mean potential temperature, A is the Earth's surface area,
148 L_f is the latent heat capacity of ice, M is the total mass of ice and the subscript 'w' indicates the
149 Warm reference state. The energy stored in the ice only represents at most 10% of E . Therefore, θ
150 and E can be used almost equivalently to describe the energy content of the system. E is an energy
151 per unit area, which we express in [$Wm^{-2}yr$] ($= 3.1 \times 10^7 Jm^{-2}$) to aid the comparison with the
152 energy extracted by volcanic eruptions. For reference, the 1991 Mount Pinatubo eruption imposed
153 a globally-averaged forcing of approximately $-4 Wm^{-2}$ at the TOA for approximately one year,
154 thus equivalent to an energy extraction of $-4 Wm^{-2}yr$.

155 Figure 1 shows that the Warm and Cold reference states have a large energetic gap (~ 2500
156 $Wm^{-2}yr$), which is a significant barrier to overcome for any transition between them. The en-
157 ergy gap between the Cold reference state and Waterbelt climates is smaller ($\sim 700 Wm^{-2}yr$) but
158 significant enough to distinguish them energetically, owing to the existence of a tropical thermo-
159 cline in the former, but not in the latter. On the other hand, the Waterbelt and Snowball states are

160 not energetically distinguishable, because most of the ocean is at freezing temperature in both the
161 states.

162 Figure 2 shows cross-sections of ocean potential temperature and overturning streamfunction,
163 along with the sea ice edge latitude and ocean heat transport (OHT) for various stable states of
164 our model. The shallow subtropical cells (STCs) are driven by the trade winds, which act upon
165 the temperature gradient of the thermocline to transport heat to the mid-latitudes. This heat flux
166 allows the stabilization of the sea ice edge and facilitates the realization of multiple equilibria in
167 the model (see Rose and Marshall (2009), Ferreira et al. (2011) and Rose (2015)). In the Warm
168 state, the meridional heat transport by the oceans reaches high latitudes in the NH, but only mid-
169 latitudes in the SH. The temperature of the deep ocean (below 1000 m) is everywhere above 6
170 °C, including at the poles where fresh surface waters allow a temperature inversion with a surface
171 colder than the abyss. In the Cold state, all the waters below 1200 m and polewards of 50° latitude
172 in both hemispheres (~ 50% of the total ocean volume) are at the freezing point. This results from
173 temperature-induced convection having to bring the entire water column to the freezing point
174 before ice can grow at the surface (see Rose et al. (2013)). The thermocline, however, remains
175 well stratified, supporting poleward heat transport by the subtropical cells, which arrests the sea
176 ice in the mid-latitudes. The maximum strength of poleward heat transport in both the Warm and
177 Cold states is order 2 PW, peaking around 20° latitude. In the Waterbelt state, the thermocline
178 stratification is eroded and the sea ice extends further equatorward, until only a shallow (~ 300
179 m) surface layer of the tropical ocean remains above freezing and the ice edge reaches around 25°
180 latitude in both hemispheres. The strength of poleward heat transport falls to 1.2 PW and the peak
181 moves equatorward to 10° latitude. Finally, in the Snowball, OHT is essentially reduced to zero

182 and the entire ocean is at the freezing point. In the following section, we explore the timescales
183 associated with changes between these states.

184 *b. Triggering transitions between equilibrium states*

185 In this section, we conduct step (constant) forcing simulations in our climate model with the
186 aim of initiating transitions between the various climate states presented in Section 3(a). Figure
187 3 shows these results on a bifurcation diagram, where each scatter represents the NH sea ice
188 latitude in the equilibrated state of a given simulation with forcing F . This forcing magnitude is
189 expressed with respect to the reference solar constant $S_0 = 341.5 \text{ Wm}^{-2}$. Simulations start from
190 either the Warm (red circles), Cold (blue squares), Waterbelt (green triangle) or Snowball (black
191 diamond) states. The solid lines describe the range over which these states exist, with the same
192 color convention. The individual states labelled ‘W’ (Warm), ‘C’ (Cold) and ‘S’ (Snowball) are
193 chosen as reference climates because they exist for $F = 0$.

194 (i) Warm start

195 Starting from ‘W’, a small step forcing of -1.5 Wm^{-2} induces a slow transition to the Cold
196 equilibrium over several thousand years. This implies that the Warm reference state is at the edge
197 of a critical threshold and is thus particularly sensitive to changes in its radiative budget. Larger
198 forcings of -7 Wm^{-2} and -11 Wm^{-2} both lead to a Cold equilibrium and a forcing of -36 Wm^{-2}
199 produces a Snowball. We also force the Warm reference state with a positive forcing of $+3 \text{ Wm}^{-2}$,
200 which leads to a Very Warm (‘VW’) climate that has no ice anywhere on the globe, a global
201 mean ocean potential temperature of $14 \text{ }^\circ\text{C}$ and a global mean SST of $24 \text{ }^\circ\text{C}$. We find no stable
202 states between 90° and 45° NH sea ice extent. The absence of a stable climate with a small ice
203 cap, known as the small ice instability (SICI), has been discussed in the context of simple EBMs

204 (e.g. Held and Suarez (1975) and North (1985)) and more sophisticated models (e.g. Huang
205 and Bowman (1992), Matteucci (1993), Lee and North (1995), Morales Maqueda et al. (1998)
206 and Langen (2004)). While these studies concluded that the SICI tends to disappear with better
207 representation of continental geometry, unforced variability, ice sheets and ice dynamics, further
208 work would be required to investigate the lack of a small ice cap climate in the model used here.

209 (ii) Cold start

210 Starting from ‘C’, we find that step forcings of -2, -3, -5 and -9 Wm^{-2} lead to progressively
211 colder climates without abrupt state transitions. For $F_{c/s} = -20 Wm^{-2}$, the climate initially transi-
212 tions to a Cold climate that remains stable for about 150 years, but then collapses into a Snowball.
213 Between $F_{wb} = -5 Wm^{-2}$ and $F_{c/s}$, we find Cold climates with $\theta < -1.5$ °C and tropical sea ice,
214 which we refer to as Waterbelts. Starting from such a Waterbelt climate (‘WB’) and relaxing the
215 forcing to 0, we find that the system returns to ‘C’. Finally, we conduct warming experiments
216 starting from ‘C’ with $F = +1.5$ and $+8 Wm^{-2}$, which lead back to a Warm climate. We conclude
217 that there is no identifiable hysteresis loop between the Cold and Warm branches.

218 (iii) Snowball start

219 Starting from a Snowball, we relax F to 0 and find that the climate remains in a Snowball state
220 (‘S’). Thus, the Cold branch is not directly accessible from a Snowball state. Starting from ‘S’,
221 we attempt to exit the Snowball state by imposing a forcing of $+7 Wm^{-2}$, but find that the surface
222 remains frozen everywhere. We expect that a larger positive forcing could overcome the strong ice-
223 albedo feedback and bring the system back to the Warm branch, but the magnitude of this forcing
224 is not quantified in this study. Note that if this threshold large enough however, the climate may
225 not stabilize into a Warm state, and instead transition directly to a moist or runaway greenhouse
226 (Yang et al. (2017)).

227 The plot on the right of Figure 3 summarizes these results in a simplified schematic (not to scale).
228 The arrows show two hypothetical paths along the bifurcation diagram. Starting from Warm (red
229 arrows) and slowly reducing the solar constant, the system would reach the Warm/Cold transition
230 threshold $F_{w/c} \sim -1.5 \text{ Wm}^{-2}$ and move down to the Cold branch. The system would then smoothly
231 transition to a Waterbelt-like climate around $F_{wb} \sim -5 \text{ Wm}^{-2}$, before reaching the Cold/Snowball
232 threshold $F_{c/s} \sim -20 \text{ Wm}^{-2}$. From a Snowball state, a large increase in the solar constant would
233 be required to switch back to the Warm state and complete the loop. When starting from the Cold
234 branch (blue arrows) and increasing the solar constant, the system can move to the Warm branch
235 without any hysteresis. In the Appendix, we further interpret this bifurcation diagram in terms
236 of a 1D EBM developed by Rose (2015), which shows characteristics that are reminiscent of our
237 climate model.

238 **4. Transition timescales between equilibrium states**

239 *a. Transitions in response to step forcings*

240 Figure 4 shows state transition times in the climate model for the step simulations starting from
241 the Warm (red) and the Cold (blue) reference states as a function of the forcing magnitude. These
242 are the same experiments as used in Figure 3. State transitions to both a Waterbelt climate and
243 a Snowball are considered. As expected, the transition time shortens as the forcing magnitude
244 increases, and there is a minimum threshold forcing below which no transition occurs. Transitions
245 from the Warm state take longer than from Cold (for the same forcing) because more energy must
246 be extracted in the process. Voigt and Marotzke (2010) (subsequently VM2010) argued that as
247 the planet approaches a Snowball, deep convection and the transport of cold waters into the abyss

248 eventually lead to a well-mixed ocean. This prompted them to adopt the following 1-box model
249 (here expressed in terms of anomalies) to estimate state transition times:

$$\rho c H \frac{dT(t)}{dt} = F(t) - \lambda T(t), \quad (2)$$

250 where F is the TOA forcing, T is the temperature anomaly relative to the starting state, λ is the
251 climate feedback parameter and H is the ocean depth relevant to the transition. The model does
252 not take account of the change in albedo as the transition occurs since all parameters are constant
253 in time. The solution for the step response (constant F) of Eq. (2) is:

$$T(t) = T_{eq}(1 - e^{-t/\tau}) \quad (3)$$

254 where the system timescale τ is given by:

$$\tau = \frac{\rho c H}{\lambda} \quad (4)$$

255 and the equilibrium climate sensitivity is

$$T_{eq} = \frac{F}{\lambda}, \quad (5)$$

256 where here F is negative, corresponding to extraction of energy.

257 As we now explore, state transition times in our climate model are well captured by the 1-
258 box model, when considering the difference in potential temperature between the initial and final
259 states $\Delta\theta$. The time taken by the 1-box model to achieve a temperature difference $\Delta\theta$ through a
260 step forcing F is obtained from Eq. (3) as follows:

$$t_f = \tau \times \ln\left(\frac{T_{eq}}{T_{eq} - \Delta\theta}\right), \quad (6)$$

261 From Eq. (5), the forcing required to obtain a temperature response $\Delta\theta$ at equilibrium is:

$$F_{min} = \lambda\Delta\theta, \quad (7)$$

262 It follows that forcings weaker than F_{min} cannot achieve this temperature change, even when
 263 sustained indefinitely. Therefore, F must be larger than or equal to F_{min} to achieve a temperature
 264 change $\Delta\theta$.

265 One can also estimate the efficiency of energy transfer required to achieve $\Delta\theta$, as a function of
 266 forcing magnitude. The total energy E_{tot} supplied by the forcing during the transition is:

$$\Delta E_{tot} = F \times t_f,$$

267 where we ignore the energy stored in the atmosphere, land and sea ice. From Eq. (1), the net
 268 energy ΔE_{net} extracted from the system for a temperature change $\Delta\theta$ is:

$$\Delta E_{net} = \rho c H \Delta\theta.$$

269 The efficiency of energy extraction ε is then:

$$\varepsilon = \frac{\Delta E_{net}}{\Delta E_{tot}} = \frac{\Delta\theta}{T_{eq}} \ln\left(\frac{T_{eq}}{T_{eq} - \Delta\theta}\right)^{-1}.$$

270 As the forcing amplitude increases ($F \rightarrow -\infty$), the efficiency ε tends to 1, but drops to 0 as
 271 F tends toward F_{min} . For large forcings, climatic feedbacks have limited time to act, and hence

272 the energy extraction occurs efficiently. Conversely, as the forcing magnitude decreases, the cli-
 273 matic feedbacks have enough time to counter the effect of the forcing, and as F drops below F_{min} ,
 274 the feedbacks become too strong to allow a temperature change $\Delta\theta$ altogether. In the following
 275 paragraphs, we investigate to what extent these simple ideas apply to the climate model transitions.

276 For simulations starting from Warm, the temperature anomalies spread into every part of the
 277 ocean, including the abyss. Thus, the relevant depth H of the 1-box model is $H_{tot} = 2416$ m (the
 278 total area-averaged depth of the ocean). The climate sensitivity parameter in the Warm reference
 279 state is found using the method outlined in Gregory et al. (2004) (details in SI), which gives $\lambda_w =$
 280 $0.72 \text{ W m}^{-2} \text{ K}^{-1}$. This value is associated with the SST response of the model, but the assumption
 281 of a well-mixed ocean allows us to extend it to the ocean-mean temperature. For a transition to
 282 a Snowball, the initial temperature is $\theta_i = 8.3^\circ \text{ C}$ and the final temperature is $\theta_f = -1.8^\circ \text{ C}$, the
 283 freezing point of water. Inserting these values into Eq. (6) gives the red curve in Figure 4, which
 284 is a reasonable approximation to the coupled model results.

285 Figure 4 also shows (in orange squares) the Snowball transition times obtained by VM2010,
 286 when starting from a modern-day climate in a comprehensive GCM. To facilitate comparison with
 287 our simulations starting from Warm, we scale the VM2010 timescales by a factor f_{vm} , to account
 288 for the different heat capacities of the two models:

$$f_{vm} = \frac{H_{tot}(\theta_w - \theta_f)}{H_{vm}(\theta_{vm} - \theta_f)},$$

289 where $H_{vm} = 2603$ m is a realistic globally-averaged depth for the modern ocean (including
 290 land surfaces) and $\theta_{vm} = 4.4^\circ \text{ C}$, as reported in VM2010. This gives a scaling parameter $f_{vm} =$
 291 1.5. Figure 4 shows that the transition timescales obtained by VM2010 are larger than the ones

292 corresponding to the Warm start simulations and this difference is accentuated by the factor f_{vm} .
293 Using the 1-box model with the parameters provided by VM2010 (orange line), one finds the
294 effective climate feedback parameter in their model to be $\lambda_{vm} = 3.3 \text{ Wm}^{-2}\text{K}^{-1}$ (see SI). This is
295 significantly larger than λ_w and results in longer transition times. Note that λ_{vm} is larger than the
296 climate feedback parameters typically reported by state-of-the-art GCMs ($\sim 1 \text{ Wm}^{-2}\text{K}^{-1}$) such
297 as the one used in VM2010. However, a direct comparison may not be possible because λ_{vm} is
298 obtained from a 1-box model fit to the Snowball transition times associated with θ , rather than
299 from the more conventional ‘Gregory’ method associated with surface temperatures. Therefore,
300 λ_{vm} may encapsulate different climate processes than typical feedback parameters. In particular,
301 the representation of non-linear atmospheric feedbacks (e.g. clouds, water vapor, etc) and the
302 restructuring of the ocean may differ.

303 In the simulations starting from Cold, the temperature anomaly spreads into the part of the ocean
304 that is not already at the freezing temperature, namely the tropical thermocline. The relevant ocean
305 depth is the top 1000 m (approximately), which has an average potential temperature of $3.1 \text{ }^\circ\text{C}$.
306 The climate feedback parameter corresponding to the Cold reference state is again obtained by the
307 ‘Gregory’ method and found to be somewhat higher than for Warm: $\lambda_c = 0.95 \text{ Wm}^{-2}\text{K}^{-1}$ (see
308 details in SI). This corresponds to a timescale of 159 years (see Section 1). Using these values
309 along with $\theta_i = 3.1 \text{ }^\circ\text{C}$ and $\theta_f = -1.8 \text{ }^\circ\text{C}$ in Eq. (6) gives the solid green line in Figure 4. Overall,
310 the box model can capture the climate model’s transition times starting from Cold, but tends to
311 underestimate them as F approaches the threshold forcing.

312 *b. Transitions in response to volcanic impulse forcings*

313 1) SINGLE ERUPTIONS

314 We now investigate the behavior of the climate model following large idealized volcanic erup-
315 tions. The largest eruption simulated from the Warm state has a magnitude of $F = -105 \text{ Wm}^{-2}$,
316 which is on the same order as estimates of the Toba mega-eruption (e.g. Jones et al. (2005)). In
317 the year following the simulated eruption, the global-mean SST drops by $5.4 \text{ }^\circ\text{C}$, the global sea ice
318 fraction increases by 2% and both quantities recover their original values within 75 years. We also
319 conduct a simulation of comparable magnitude ($F = -89 \text{ Wm}^{-2}$) starting from Cold, which leads
320 to a global-mean SST drop of $3.1 \text{ }^\circ\text{C}$, a shift in the ice edge latitude from 44.4° to 42.2° (a 4%
321 increase in sea ice fraction) and a recovery within 400 years. Despite the large magnitude of the
322 forcings considered here, the net energy extracted from the system ($\sim 100 \text{ Wm}^{-2}\text{yr}$) is not large
323 enough to cause a shift in climate equilibrium (see Figure 1). The longer recovery time for SST
324 and sea ice fraction in the Cold start eruption is likely due to a stronger ice albedo feedback, since
325 the Cold state has a larger sea ice fraction (33%) than the Warm state (11%). However, we now
326 show that unlike the recovery times of surface quantities, the timescales associated with the global
327 mean ocean potential temperature θ are larger in the Warm state than the Cold one.

328 Figure 5 shows timeseries of θ for all the single eruption simulations conducted in this study.
329 The experiments are run until θ relaxes back to within the 2σ levels of unforced variability. One
330 can estimate the peak cooling θ_{peak} at the end of the first year by equating the energy extracted by
331 the forcing to the change in heat content of the ocean, and neglecting the effects of the feedbacks
332 as follows:

$$\theta_{peak} \approx \frac{F \Delta t}{\rho c H_{tot}}, \quad (8)$$

333 where Δt is the forcing duration, which is assumed small compared to the timescale associated
 334 with climatic feedbacks. Eq. (8) is a good approximation for all the simulations shown in Figure
 335 5, irrespective of how deep the anomaly penetrates into the ocean.

336 For Cold starts, we consider two eruptions with $F = -89$ and -29 Wm^{-2} (blue and purple curves
 337 respectively). Because the deep ocean is already at the freezing temperature in the starting state,
 338 the temperature anomaly remains within the tropical thermocline. When normalized with respect
 339 to θ_{peak} (Figure 5b), both responses follow the same decay, which can be fit by a decaying expo-
 340 nential with an e-folding time of $\tau_c = 159$ years (blue dotted line). According to the 1-box model,
 341 the ocean depth associated with this timescale is (see Eq. (4)):

$$H_c = \frac{\lambda_c \tau_c}{\rho c}, \quad (9)$$

342 with $\lambda_c = 0.95 \text{ Wm}^{-2}\text{K}^{-1}$ corresponding to the climate feedback for the Cold state. This gives
 343 $H_c = 1149\text{m}$ (roughly 47 % of the total ocean depth).

344 For Warm start simulations, Figure 5(b) shows that forcing pulses of magnitude $F = -35$ and -105
 345 Wm^{-2} lead to a relaxation back to equilibrium over several thousand years (orange and red curve,
 346 respectively). The normalized plot shows that the two curves follow a similar path to recovery,
 347 but the one corresponding to $F = -35 \text{ Wm}^{-2}$ reaches background noise levels within 2000 years,
 348 versus at least 5000 years for $F = -105 \text{ Wm}^{-2}$. We therefore choose to fit to the $F = -105 \text{ Wm}^{-2}$
 349 experiment and find that the following two-exponential model gives a good approximation of the
 350 impulse response (red dotted line):

$$T_i^{(w)}(t) = T_1 e^{-t/\tau_{w1}} + T_2 e^{-t/\tau_{w2}}, \quad (10)$$

351 with $T_1 = -0.10^\circ\text{C}$, $\tau_{w1} = 500$ years, $T_2 = -0.13^\circ\text{C}$ and $\tau_{w2} = 5911$ years.

352 The millennial-scale decay τ_{w2} cannot be captured by the 1-box model, since the longest
 353 timescale that can arise from Eq. (4) is 443 years, when using the full ocean depth $H = 2416$
 354 m and the inferred climate sensitivity parameter $\lambda_w = 0.72 \text{ Wm}^{-2}\text{K}^{-1}$. To better understand the
 355 origin of τ_{w2} , we conduct an additional three numerical experiments with: (i) a smaller magnitude
 356 F , (ii) a positive F , and (iii) a large negative F starting from the Very Warm state (see Figure 3):

357 (i) When F is reduced to -11 Wm^{-2} with a Warm start (yellow curve), the magnitude of the
 358 perturbation is not large enough for the θ anomaly to remain outside the range of natural variability
 359 for more than a couple of decades. The ocean temperature anomalies remain in the top 1000 m
 360 and are rapidly dissipated by climatic processes near the surface. This suggests that there is a
 361 minimum amount of forcing required (somewhere between -11 and -35 Wm^{-2}) to induce the
 362 millennial timescale of decay in θ .

363 (ii) A positive forcing experiment was conducted with $F = +31 \text{ Wm}^{-2}$ (black curve), which
 364 likely does not correspond to a particular geophysical mechanism, but is useful for assessing the
 365 asymmetry in our model's response between warming and cooling. Unlike in the corresponding
 366 negative forcing case (-35 Wm^{-2}), the decay of θ does not have a millennial timescale as it reaches
 367 background noise levels within less than 1000 years.

368 (iii) To assess the sensitivity to the starting state, a mega-eruption simulation with $F = -108$
 369 Wm^{-2} was conducted from the Very Warm state (pink curve). In this experiment, θ responded

370 with an e-folding time of 437 years, which corresponds to the decay timescale of the 1-box model
371 when considering the full depth of the ocean (pink dotted line).

372 In the following paragraph, we briefly explore aspects of ocean dynamics that can lead to the
373 millennial decay timescale τ_{w2} . Figure 6 displays vertical profiles of ocean potential temperature
374 for a subset of the single eruptions simulations conducted for this study. Panel (a) shows the F
375 $= -105 \text{ Wm}^{-2}$ simulation starting from Warm. After 100 years, the temperature profile exhibits
376 two peaks in cooling; the first around 500 m depth and the second at the bottom of the ocean. The
377 shallower peak is likely a result of anomalously cold water parcels being driven down into the ther-
378 mocline by Ekman pumping in the mid-latitudes. This mechanism can shield the cold temperature
379 anomaly away from atmospheric damping processes acting at the surface for decades to centuries
380 (e.g. Stouffer (2004), Stenchikov et al. (2009), Gupta and Marshall (2018)). The peak cooling in
381 the abyss is set by enhanced deep convection around the poles, particularly at the sea ice margin
382 in the SH (see Figure S2). After 500 years, the peak cooling in the thermocline is damped away
383 by a combination of atmospheric feedbacks and mixing into the deeper ocean. At that time, the
384 temperature anomaly profile is almost linear with depth and the mixed layer temperature anomaly
385 reaches unforced variability levels ($-0.1 \text{ }^\circ\text{C}$). The subsequent evolution of the temperature profile
386 occurs over 1000-year timescales, as the deep ocean temperature anomaly slowly diffuses back up
387 toward the surface. This upward diffusion process is illustrated using a simple 1D ocean diffusive
388 model with constant diffusivity $\kappa = 3 \times 10^{-5} \text{ m}^2\text{s}^{-1}$ (the uniform background value used in our
389 coupled model) and boundary conditions ensuring no flux at the bottom of the ocean and a tem-
390 perature anomaly fixed to 0 at the top. The latter implicitly assumes that climatic feedbacks at the
391 surface act on much shorter timescales than the various ocean processes bringing the temperature
392 anomaly back up. We initialize the 1D model with a linear temperature profile, roughly corre-

393 sponding to the temperature anomaly profile found in our climate model at $t = 500$ years. The 1D
394 model temperature evolution (in the dotted lines) shows a roughly similar relaxation behavior to
395 the coupled model and has a timescale that scales with H^2/κ , which is $O(1000)$ years).

396 Panel (b) shows θ anomaly profiles for the $F = -35 \text{ Wm}^{-2}$ impulse simulation starting from
397 Warm. At year 100, there is again a peak cooling around 500 m depth and a small peak in the abyss.
398 Figure S2 shows signatures of Ekman pumping transporting cold waters into the thermocline and
399 enhanced deep convection in the SH high latitudes, although not as large as in (a). Subsequently,
400 diffusive processes flatten the temperature profile and the deep temperature anomalies reach back
401 up to the surface over several thousands of years.

402 Panel (c) shows temperature anomaly profiles for $F = +31 \text{ Wm}^{-2}$ starting from Warm. After
403 100 years, mid-latitude Ekman pumping has driven warm temperature anomalies down into the
404 thermocline. However, a smaller fraction of the anomaly than in (b) penetrates into the deep
405 ocean, due to the higher buoyancy of these anomalously warm waters. This results in an overall
406 ocean relaxation timescale of several hundred years only.

407 Panel (d) shows temperature anomaly profiles for $F = -108 \text{ Wm}^{-2}$ starting from Very Warm.
408 After 100 years, there is a large peak cooling at the surface and a small one in the abyss. Some
409 of the temperature anomaly has penetrated into the thermocline, but the surface cooling has not
410 been damped as significantly as in (a). To explain this behavior, one should note that the Very
411 Warm state does not contain ice anywhere on the globe. The impulse cooling promotes sea ice
412 formation in the SH, but the resulting deep convection at the ice margin is not strong enough to
413 carry a large volume of cold waters into the abyss (see Figure S2). In the mid-latitudes and the

414 tropics, a fraction of the temperature anomaly does penetrate into the deeper ocean, but it is a
415 smaller share of the total cooling than in (a) and (b).

416 In summary, the millennial decay timescale τ_{w2} is a result of cold temperature anomalies reach-
417 ing the deepest layers of the ocean and slowly diffusing upward over several thousand years. These
418 anomalies can reach the seafloor by enhanced deep convection in the SH high latitudes over the
419 first few decades after the eruption. Notably, the millennial timescale does not arise for a positive
420 impulse or when starting from the Very Warm state.

421 2) SUCCESSION OF ERUPTIONS

422 We now investigate how the long oceanic timescales can favor a large build up of the cooling
423 response and potentially initiate state transitions when forced by repeated volcanic eruptions. We
424 first establish whether the transition behavior for volcanic eruptions of magnitude F and duration
425 Δt (assumed 1 year) repeated every τ_i years is equivalent to that of a step simulation with average
426 forcing F_{av} :

$$F_{av} = \frac{F \Delta t}{\tau_i}. \quad (11)$$

427 Figure 7 shows the globally-averaged θ and sea ice fraction evolution for two simulations in
428 which the model is forced by an idealized eruption every $\tau_i = 10$ years, with $F = -105 \text{ Wm}^{-2}$
429 starting from Warm and $F = -89 \text{ Wm}^{-2}$ starting from Cold. For comparison, we also consider step
430 simulations with $F_{av} = -11 \text{ Wm}^{-2}$ starting from Warm and $F_{av} = -9 \text{ Wm}^{-2}$ starting from Cold.
431 The results show that the θ and sea ice fraction timeseries obtained from the repeated eruption
432 simulations closely follow the corresponding step simulations, for both Warm and Cold starts.
433 All simulations eventually transition to a Waterbelt state with approximately 60% ice fraction and

434 the sea ice edge stabilizes around 27° latitude in both hemispheres. The step response is a good
435 approximation for repeated eruptions because the interval between them is much smaller than the
436 ocean relaxation timescales, and because each incremental cooling from a given eruption is much
437 smaller than the overall $\Delta\theta$.

438 Figure 7 also shows that the 1-box model of Eq. (2) faithfully represents the evolution of θ in
439 all the cases considered. There are non-linearities associated with the transition, but since those
440 only significantly affect θ near the freezing point ($\theta_f = -1.8^\circ\text{C}$), the 1-box model provides a
441 good estimate of the state transition times. For the Cold start simulations, both single eruption
442 and step simulations were well approximated by the 1-box model with timescale $\tau_c = 159$ years
443 and a climate feedback parameter $\lambda_c = 0.95 \text{ Wm}^{-2}\text{K}^{-1}$ (see Sections and a and 1). For Warm
444 start simulations, however, there is an apparent discrepancy between the two-timescale model
445 used in Figure 5 and the single timescale model used in Figure 7. This is resolved by noting
446 that here, a state transition occurs after 550 years, which is too short to activate the millennial
447 timescale. Therefore, the 1-box model is a good approximation for transitions occurring within
448 several centuries, but otherwise the 2-timescale model is more appropriate.

449 In Figure 8, we explore the state transition times for repeated uniform eruptions over a range
450 of impulse forcings F (lasting 1 year) and eruption intervals τ_i . One can estimate the transition
451 threshold by assuming a step response with constant forcing F_{av} because the system timescales
452 are much longer than the interval between eruptions. This implies that scenarios with the same
453 F_{av} have the same transition time, which results in the straight contours in Figure 8. The dotted
454 lines show the following transition threshold boundaries: Warm/Cold in black ($F_{w/c} = -1.5 \text{ Wm}^{-2}$),
455 Cold/Waterbelt in red ($F_{wb} = -5 \text{ Wm}^{-2}$) and Cold/Snowball in white ($F_{c/s} = -20 \text{ Wm}^{-2}$).

456 For the Cold start case, we assume a 1-box model with timescale $\tau_c = 160$ years and can thus es-
457 timate transition times to either a Waterbelt or Snowball climate using Eq. (6) and the parameters
458 calculated in Section 4(a), with $F = F_{av}$. As noted that Section, the box model tends to underes-
459 timate the GCM transition timescales for Cold start simulations when F is of low magnitude, so
460 the results of Figure 8(a) should be regarded as a lower bound. When the repeated eruptions start
461 from Warm, the transition times can be estimated similarly, but in this case there are two timescales
462 (τ_{w1} and τ_{w2}) involved in the response. When the forcing is large enough for a transition to occur
463 within several hundred years, Figure 7 showed that the 1-box model was a suitable approximation.
464 However, a more general estimate of the step response can be obtained by integrating Eq. (10) and
465 scaling it appropriately to obtain the two-timescale step response from Warm:

$$T_s^{(w)}(t) = \frac{F}{F_{ref}} [T_1 \tau_{w1} (1 - e^{-t/\tau_{w1}}) + T_2 \tau_{w2} (1 - e^{-t/\tau_{w2}})], \quad (12)$$

466 where $F_{ref} = -105 \text{ Wm}^{-2}$. The time taken to transition from an initial temperature $\theta_i = 8.3^\circ \text{ C}$
467 to the final temperature θ_f is calculated numerically using Eq. (12) and shown in Figure 8(b).
468 For transitions to either a Waterbelt or Snowball climate, the final temperature is $\theta_f = -1.8^\circ \text{ C}$
469 (the freezing point), whereas for transitions to the Cold state it is $\theta_f = 0.5^\circ \text{ C}$. Note that we only
470 consider transition times smaller than 10^4 years, because over longer timescales, greenhouse gas
471 emissions from volcanic eruptions may start to overcome the cooling (e.g. Walker et al. (1981)).

472 Figure 8 shows that transition to a Snowball requires a sequence of almost continuous Toba-like
473 events ($\sim -100 \text{ Wm}^{-2}$) for at least several decades, even when starting from a Cold climate. This
474 differs from the results of Macdonald and Wordsworth (2017), who suggested that such a transition
475 could occur within 3 years for volcanic eruptions with a peak forcing as weak as -10 Wm^{-2} . This
476 difference arises because the heat capacity of their model consists of the mixed layer depth of the

477 ocean (50 m), whereas in our climate model, the entire tropical thermocline (~ 1000 m) plays a
478 role when starting from Cold. Transitions to a Waterbelt climate may occur for a weaker F_{av} , but
479 over several hundred years for a Cold start and around one or two thousand years for a Warm start.
480 In this climate model, such Waterbelt-like states do not exist for $F = 0$ (see Figure 3), so the system
481 would relax back to Cold when the eruptions stopped. Nevertheless, the hysteresis associated with
482 Waterbelt states may differ between models (e.g. Rose (2015)), and therefore the possibility of
483 a long-term transition to such a state is still plausible. Finally, volcano-induced transitions from
484 Warm to Cold may occur for small magnitude forcings ($\sim -1.5 \text{ Wm}^{-2}$), due to the proximity of the
485 Warm reference state to a transition threshold. However, such transitions take several thousands
486 of years, during which the build-up of greenhouse gases from intense volcanic activity could start
487 mitigating the cooling effect.

488 5. Conclusions

489 Our study has explored transitions between the global equilibria of a complex coupled climate
490 model with representations of atmosphere, ocean, sea ice and land. We study whether cooling
491 associated with volcanic eruptions - acting alone (single pulse) or in concert (repeating pulse or
492 step) - could trigger transitions between equilibrium states. Although the models employed are
493 rather idealized, we offer the following general conclusions that hopefully do not depend on those
494 idealizations:

- 495 1. A series of Toba-like events ($F \sim -100 \text{ Wm}^{-2}$) must occur almost continuously for a min-
496 imum of several decades to initiate a transition to a Snowball climate by volcanic cooling
497 acting alone. This is a significantly longer forcing period than reported by Macdonald and
498 Wordsworth (2017), because over the large part of the global ocean, the entire water column
499 (rather than just the mixed layer) must reach the freezing temperature of sea water before

500 ice can form at the surface. This result is consistent with the work of Voigt and Marotzke
501 (2010) and Voigt et al. (2011). The relevant system timescales are associated with the full
502 ocean depth when starting from a Warm climate and the tropical thermocline when starting
503 from a Cold one. Assuming that volcanic forcings are no greater in magnitude than Toba-like
504 events, the interval between eruptions must be on the order of years to decades (much smaller
505 than the oceanic timescales) to successfully initiate any state transition between them. Con-
506 sequently, the transition behavior can be predicted from the time-average forcing F_{av} without
507 knowledge of the detailed history of volcanic forcing.

- 508 2. The presence of multiple equilibria in the climate system could in theory enable a multistage
509 transition to a Snowball. Indeed, if the climate were already in a stable Cold state with sea
510 ice extending down into the mid-latitudes, then volcanic cooling could more readily initiate
511 a Snowball transition, since only the tropical thermocline would remain to be brought to
512 the freezing temperature. Nevertheless, decades of intense volcanic cooling would still be
513 required, even in this most favorable case.
- 514 3. The proximity of the equilibrium state to a transition threshold controls the amount of forcing
515 required to initiate a transition. In our model, the Snowball transition threshold is $F_{c/s} = -20$
516 Wm^{-2} (a 5.8% reduction in incoming solar radiation with respect to the modern constant).
517 This is comparable to the values found in other studies (e.g. Voigt and Marotzke (2010),
518 Voigt et al. (2011), Yang et al. (2012)). The Warm reference state, which resides close to a
519 critical threshold, may evolve into a Cold state for a forcing as small as $-1 Wm^{-2}$, although
520 this forcing must be sustained for several thousands of years.
- 521 4. The most extreme climates on the Cold branch of our bifurcation diagram are analogous to
522 Waterbelt (or Slushball) climates, in which sea ice extends down to the tropics. The energy

523 required to access such states is similar to that of a Snowball, since both have a mean ocean
524 temperature close to freezing. The threshold forcing for the Waterbelt state ($F_{wb} = -5 \text{ Wm}^{-2}$)
525 is significantly lower than for a Snowball ($F_{c/s} = -20 \text{ Wm}^{-2}$), but if the forcing is relaxed
526 after a Waterbelt transition, the system smoothly returns to a climate with no tropical sea ice.
527 This differs from the results of Rose (2015), who find two distinct branches for the Cold and
528 Waterbelt states, and a significant amount of hysteresis associated with the latter.

- 529 5. A simple 1-box model can capture transition times for both Warm and Cold start simulations
530 relatively well. However, close to the Warm/Cold transition threshold, the climate model
531 exhibits a millennial decay timescale that cannot be explained by the assumption of a well-
532 mixed ocean. This is caused by enhanced deep convection in the SH, which produces cold
533 temperature anomalies in the abyssal ocean that diffuse back up to the surface over thousands
534 of years. In this case, a 2-box model that includes this millennial decay timescale provides
535 better estimates of transition times.

536 *Acknowledgments.* The authors acknowledge support from the MIT-GISS collaborative agree-
537 ment (NASA) and are grateful for informative conversations with Brian E. J. Rose.

538 APPENDIX

539 **Interpretation in terms of a Budyko-Sellers energy balance model**

540 A simple Budyko-Sellers energy balance model (EBM) modified to include the effect of OHT
541 (as in Rose and Marshall (2009)) can be used to illuminate the multiple equilibria found in the
542 climate model. We employ the following model, developed by Rose (2015), which describes the
543 zonal-mean energy balance of the planet in terms of a characteristic surface temperature T :

$$Q_0(1 + s_2 P_2(x))a(x, T) - (A + BT(x)) + K_a \frac{d}{dx} \left((1 - x^2) \frac{dT(x)}{dx} \right) + F_o(x) = 0, \quad (\text{A1})$$

544 where $x = \sin(\phi)$ and ϕ is latitude, $T(x)$ is the zonal-mean equilibrium surface temperature
 545 [$^{\circ}$ C], K_a is a coefficient of large-scale heat diffusion for the atmosphere [$Wm^{-2}K^{-1}$], B is the
 546 longwave radiative damping [$Wm^{-2}K^{-1}$], Q_0 is the solar constant (divided by 4), $F_o(x)$ is OHT
 547 convergence and $a(x, T)$ is a non-linear co-albedo function that depends strongly on T. The term
 548 $Q_0(1 + s_2 P_2(x))$ gives a reasonable spatial distribution of the incoming radiation, where $P_2(x)$ is the
 549 second Legendre polynomial and $s_2 = -0.48$. The OHT is held constant in time and parameterized
 550 as follows:

$$H_o(x) = \Psi \sin(\phi) \cos(\phi)^{2N} = \Psi x(1 - x^2)^N, \quad (\text{A2})$$

551 where N is a positive integer and Ψ is a constant (in units of PW) setting the amplitude of OHT.
 552 The parameter N controls the shape of the OHT profile, with higher values shifting the peak of
 553 OHT and its convergence closer to the equator and thus helping the stabilization of the ice edge at
 554 lower latitudes. The ocean heat convergence is then:

$$F_o(x) = -\frac{\Psi}{2\pi^2 R} (1 - x^2)^{N-1} (1 - x^2(2N + 1)). \quad (\text{A3})$$

555 The co-albedo switches abruptly from ice-free value (a_0) to the ice-covered (a_i), depending on
 556 the local temperature as follows:

$$a(x, T) = \begin{cases} a_0 : T(x) < T_{xi} \\ a_i : T(x) > T_{xi}. \end{cases}$$

557 A key feature is that the threshold T_{xi} is not tied to a fixed temperature, but depends on the local
 558 energy balance at the ice-water interface as follows:

$$T_{xi} = T_f - \frac{h_{min}}{k_i} F_o(x_i). \quad (\text{A4})$$

Eq. (A4) is derived by equating the vertical heat flux through the ice to the ocean heat convergence at the ice edge. The parameter h_{min} is the minimum sea ice thickness to have a substantial effect on the albedo and k_i is the thermal conductivity of sea ice. Therefore, T_{xi} represents the maximum surface temperature possible to maintain an ice thickness larger than h_{min} for a given ocean heat convergence F_o , and is used as the crude threshold between ice-free and ice-covered conditions in the EBM. Incorporating this piece of ice physics helps stabilize climates with intermediate ice covers.

Figure A1 shows a range of bifurcation diagrams obtained by solving the EBM with typical parameter values, as in Rose (2015). The analytical solution is obtained using the method detailed in North (1975) and the numerical solution is obtained with a Crank-Nicholson scheme. The numerical estimates only capture the stable (positive slope) states whereas the analytical solution gives all equilibria. Solutions are plotted for increasing values of $\delta = \frac{K_a}{B}$, which measures the efficiency of atmospheric meridional heat transport relative to radiative damping. Figure A1 shows that as δ increases, the slopes become steeper and thus more prone to instability, consistent with the analytical results of Held and Suarez (1975). However, as argued by Rose and Marshall (2009), the presence of OHT can help stabilize the ice edge as δ increases. Figure A1 also shows the OHT profile for $\Psi = 4$ PW and $N = 4$, which has a peak value of 0.91 PW that occurs at 22° latitude, not untypical of our own climate. We find that δ values between 0.4 and 0.5 give a bifurcation diagram with somewhat similar characteristics to the one obtained from the climate model, including steep slopes and a continuous set of stable equilibria at intermediate latitudes. The $\delta = 0.5$ curve also gives a bifurcation point close to $Q_0 = 341.5 \text{ Wm}^{-2}$, which is a feature seen in our climate model.

580 However, the stable states of this curve are not actually accessible from the warm state, as cooling
581 from the Warm branch directly leads to a Snowball.

582 **References**

583 Abbot, D. S., A. Voigt, and D. Koll, 2011: The Jormungand global climate state and im-
584 plications for Neoproterozoic glaciations. *Journal of Geophysical Research*, **116 (D18)**, doi:
585 10.1029/2011JD015927, URL <http://doi.wiley.com/10.1029/2011JD015927>.

586 Baresel, B., H. Bucher, B. Bagherpour, M. Brosse, K. Guodun, and U. Schaltegger, 2017:
587 Timing of global regression and microbial bloom linked with the Permian-Triassic bound-
588 ary mass extinction: implications for driving mechanisms. *Scientific Reports*, **7**, 43 630, doi:
589 10.1038/srep43630, URL <http://www.nature.com/articles/srep43630>.

590 Brugger, J., G. Feulner, and S. Petri, 2017: Baby, it's cold outside: Climate model simu-
591 lations of the effects of the asteroid impact at the end of the cretaceous. *Geophysical Re-*
592 *search Letters*, **44 (1)**, 419–427, doi:10.1002/2016GL072241, URL [http://doi.wiley.com/10.](http://doi.wiley.com/10.1002/2016GL072241)
593 [1002/2016GL072241](http://doi.wiley.com/10.1002/2016GL072241).

594 Budyko, M. I., 1969: The effect of solar radiation variations on the climate of the earth. *Tellus*,
595 **21 (5)**, 611–619.

596 Ferreira, D., J. Marshall, T. Ito, and D. McGee, 2018: Linking Glacial-Interglacial States to Mul-
597 tiple Equilibria of Climate. *Geophysical Research Letters*, doi:10.1029/2018GL077019, URL
598 <http://doi.wiley.com/10.1029/2018GL077019>.

599 Ferreira, D., J. Marshall, and B. Rose, 2011: Climate Determinism Revisited: Multiple Equi-
600 libria in a Complex Climate Model. *Journal of Climate*, **24 (4)**, 992–1012, doi:10.1175/
601 [2010JCLI3580.1](http://journals.ametsoc.org/doi/abs/10.1175/2010JCLI3580.1), URL <http://journals.ametsoc.org/doi/abs/10.1175/2010JCLI3580.1>.

602 Gregory, J. M., and Coauthors, 2004: A new method for diagnosing radiative forcing and climate
603 sensitivity. *Geophysical Research Letters*, **31** (3), doi:10.1029/2003GL018747, URL <http://doi.wiley.com/10.1029/2003GL018747>.

605 Gupta, M., and J. Marshall, 2018: The Climate Response to Multiple Volcanic Eruptions Mediated
606 by Ocean Heat Uptake: Damping Processes and Accumulation Potential. *Journal of Climate*,
607 **31** (21), 8669–8687, URL <http://journals.ametsoc.org/doi/10.1175/JCLI-D-17-0703.1>.

608 Held, I., and M. Suarez, 1975: Simple albedo feedback models of the icecaps. *Tellus*, **26**, 613–629.

609 Hoffman, P., A. Kaufman, G. Halverson, and D. Schrag, 1998: A neoproterozoic snowball earth.
610 *Science*, **281**, pp. 1342–1346, doi:10.1126/science.281.5381.1342.

611 Hoffman, P. F., and Coauthors, 2017: Snowball earth climate dynamics and cryogenian geology-
612 geobiology. *Science Advances*, **3** (11), e1600983, doi:10.1126/sciadv.1600983, URL <http://advances.sciencemag.org/lookup/doi/10.1126/sciadv.1600983>.

614 Huang, J., and K. P. Bowman, 1992: The small ice cap instability in seasonal energy balance
615 models. *Climate Dynamics*, **7** (4), 205–215, doi:10.1007/BF00206862, URL <http://link.springer.com/10.1007/BF00206862>.

617 Jones, G. S., J. M. Gregory, P. A. Stott, S. F. B. Tett, and R. B. Thorpe, 2005: An AOGCM simula-
618 tion of the climate response to a volcanic super-eruption. *Climate Dynamics*, **25** (7-8), 725–738,
619 doi:10.1007/s00382-005-0066-8, URL <http://link.springer.com/10.1007/s00382-005-0066-8>.

620 Kaiho, K., and N. Oshima, 2017: Site of asteroid impact changed the history of life on Earth: the
621 low probability of mass extinction. *Scientific Reports*, **7** (1), doi:10.1038/s41598-017-14199-x,
622 URL <http://www.nature.com/articles/s41598-017-14199-x>.

- 623 Langen, P. L., 2004: Multiple equilibria and asymmetric climates in the CCM3 coupled to an
624 oceanic mixed layer with thermodynamic sea ice. *Geophysical Research Letters*, **31** (4), doi:
625 10.1029/2003GL019039, URL <http://doi.wiley.com/10.1029/2003GL019039>.
- 626 Lee, W.-H., and G. North, 1995: Small ice cap instability in the presence of fluctuations. *Climate*
627 *Dynamics*, (11), 242–246, doi:10.1007/BF00215010.
- 628 Macdonald, F. A., and R. Wordsworth, 2017: Initiation of Snowball Earth with volcanic sulfur
629 aerosol emissions. *Geophysical Research Letters*, doi:10.1002/2016GL072335, URL <http://doi.wiley.com/10.1002/2016GL072335>.
- 631 Marshall, J., A. Adcroft, C. Hill, Perelman, and Heisey, 1997a: A finite-volume, incompressible
632 Navier Stokes model for studies of the ocean on parallel computers. *Journal of geophysical*
633 *research: Oceans*, doi:doi.org/10.1029/96JC02775.
- 634 Marshall, J., C. Hill, Perelman, and A. Adcroft, 1997b: Hydrostatic, quasi-hydrostatic, and
635 non-hydrostatic ocean modelling. *Journal of Geophysical Research: Oceans*, doi:10.1029/
636 96JC02776.
- 637 Matteucci, G., 1993: Multiple equilibria in a zonal energy balance climate model: The thin ice
638 cap instability. *Journal of Geophysical Research: Atmospheres*, **98** (D10), 18 515–18 526, doi:
639 10.1029/93JD01740, URL <http://doi.wiley.com/10.1029/93JD01740>.
- 640 Molteni, F., 2003: Atmospheric simulations using a GCM with simplified physical parametriza-
641 tions. I: model climatology and variability in multi-decadal experiments. *Climate Dynam-*
642 *ics*, **20** (2), 175–191, doi:10.1007/s00382-002-0268-2, URL <http://link.springer.com/10.1007/s00382-002-0268-2>.

- 644 Morales Maqueda, M. A., A. J. Willmott, J. L. Bamber, and M. S. Darby, 1998: An investigation
645 of the small ice cap instability in the Southern Hemisphere with a coupled atmosphere-sea ice-
646 ocean-terrestrial ice model. *Climate Dynamics*, **14** (5), 329–352, doi:10.1007/s003820050227,
647 URL <http://link.springer.com/10.1007/s003820050227>.
- 648 North, G., 1975: Theory of energy-balance models. *Journal of the atmospheric sciences*, **32** (11),
649 2033–2043.
- 650 North, G., 1985: The small ice cap instability in diffusive models. *Journal of the Atmospheric*
651 *Sciences*, **41** (23), 3390–3395, doi:10.1175/1520-0469(1984)041<3390:TSICII>2.0.CO;2.
- 652 Poulsen, C. J., and R. L. Jacob, 2004: Factors that inhibit snowball Earth simulation. *Paleoceanog-*
653 *raphy*, **19** (4), doi:10.1029/2004PA001056, URL <http://doi.wiley.com/10.1029/2004PA001056>.
- 654 Prueher, L., and D. Rea, 2001: Volcanic triggering of late pliocene glaciation: evidence from the
655 flux of volcanic glass and ice-rafted debris to the north pacific ocean. *Palaeogeography, Palaeo-*
656 *climatology, Palaeoecology*, **173** (3-4), 215–230, doi:[https://doi.org/10.1016/S0031-0182\(01\)](https://doi.org/10.1016/S0031-0182(01)00323-6)
657 00323-6.
- 658 Rampino, M., and S. Self, 1992: Volcanic winter and accelerated glaciation following the toba
659 super-eruption. *Nature*, **359**, 50–52.
- 660 Robock, A., 2000: Volcanic eruptions and climate. *Reviews of Geophysics*, **38**, doi:10.1029/
661 1998RG000054.
- 662 Rose, B. E. J., 2015: Stable Waterbelt climates controlled by tropical ocean heat transport: A
663 nonlinear coupled climate mechanism of relevance to Snowball Earth. *Journal of Geophys-*
664 *ical Research: Atmospheres*, **120** (4), 1404–1423, doi:10.1002/2014JD022659, URL <http://doi.wiley.com/10.1002/2014JD022659>.

666 Rose, B. E. J., D. Ferreira, and J. Marshall, 2013: The Role of Oceans and Sea Ice in Abrupt Tran-
667 sitions between Multiple Climate States. *Journal of Climate*, **26 (9)**, 2862–2879, doi:10.1175/
668 JCLI-D-12-00175.1, URL <http://journals.ametsoc.org/doi/abs/10.1175/JCLI-D-12-00175.1>.

669 Rose, B. E. J., and J. Marshall, 2009: Ocean Heat Transport, Sea Ice, and Multiple Climate States:
670 Insights from Energy Balance Models. *Journal of the Atmospheric Sciences*, **66 (9)**, 2828–2843,
671 doi:10.1175/2009JAS3039.1, URL [http://journals.ametsoc.org/doi/abs/10.1175/2009JAS3039.](http://journals.ametsoc.org/doi/abs/10.1175/2009JAS3039.1)
672 1.

673 Sellers, W. D., 1969: A global climatic model based on the energy balance of the earth-atmosphere
674 system. *Journal of applied meteorology*, doi:10.1175/1520-0450(1969)008<0392:AGCMBO>2.
675 0.CO;2.

676 Stenchikov, G., T. L. Delworth, V. Ramaswamy, R. J. Stouffer, A. Wittenberg, and F. Zeng,
677 2009: Volcanic signals in oceans. *Journal of Geophysical Research*, **114 (D16)**, doi:10.1029/
678 2008JD011673, URL <http://doi.wiley.com/10.1029/2008JD011673>.

679 Stern, R. J., D. Avigad, N. Miller, and M. Beyth, 2008: From volcanic winter to Snowball Earth:
680 An alternative explanation for Neoproterozoic biosphere stress. *Links Between Geological Pro-*
681 *cesses, Microbial Activities&Evolution of Life*, Springer, 313–337.

682 Stommel, H., 1961: Thermohaline convection with two stable regimes of flow. *Tellus*, **XI11**, 224–
683 230, URL <https://doi.org/10.1111/j.2153-3490.1961.tb00079.x>.

684 Stouffer, R. J., 2004: Time Scales of Climate Response. *Journal of Climate*, **17 (1)**, 209–
685 217, doi:10.1175/1520-0442(2004)017<0209:TSOCR>2.0.CO;2, URL [http://journals.ametsoc.](http://journals.ametsoc.org/doi/abs/10.1175/1520-0442%282004%29017%3C0209%3ATSOCR%3E2.0.CO%3B2)
686 [org/doi/abs/10.1175/1520-0442%282004%29017%3C0209%3ATSOCR%3E2.0.CO%3B2](http://journals.ametsoc.org/doi/abs/10.1175/1520-0442%282004%29017%3C0209%3ATSOCR%3E2.0.CO%3B2).

687 Timmreck, C., H.-F. Graf, S. J. Lorenz, U. Niemeier, D. Zanchettin, D. Matei, J. H. Jungclaus,
688 and T. J. Crowley, 2010: Aerosol size confines climate response to volcanic super-eruptions.
689 *Geophysical Research Letters*, **37** (24), doi:10.1029/2010GL045464, URL [http://doi.wiley.com/
690 10.1029/2010GL045464](http://doi.wiley.com/10.1029/2010GL045464).

691 Tripathi, A., and H. Elderfield, 2005: Deep-sea temperature and circulation changes at the
692 paleocene-eocene thermal maximum. *Science*, **308** (5730), 1894–1898, doi:10.1126/science.
693 1111724, URL <http://www.sciencemag.org/cgi/doi/10.1126/science.1111724>.

694 Voigt, A., and D. S. Abbot, 2012: Sea-ice dynamics strongly promote Snowball Earth initiation
695 and destabilize tropical sea-ice margins. *Climate of the Past*, **8** (6), 2079–2092, doi:10.5194/
696 cp-8-2079-2012, URL <https://www.clim-past.net/8/2079/2012/>.

697 Voigt, A., D. S. Abbot, R. T. Pierrehumbert, and J. Marotzke, 2011: Initiation of a Marinoan
698 Snowball Earth in a state-of-the-art atmosphere-ocean general circulation model. *Climate of the
699 Past*, **7** (1), 249–263, doi:10.5194/cp-7-249-2011, URL <http://www.clim-past.net/7/249/2011/>.

700 Voigt, A., and J. Marotzke, 2010: The transition from the present-day climate to a modern
701 Snowball Earth. *Climate Dynamics*, **35** (5), 887–905, doi:10.1007/s00382-009-0633-5, URL
702 <http://link.springer.com/10.1007/s00382-009-0633-5>.

703 Walker, J. C., P. B. Hays, and J. F. Kasting, 1981: A negative feedback mechanism for the long-
704 term stabilization of Earth's surface temperature. *Journal of Geophysical Research: Oceans*,
705 **86** (C10), 9776–9782.

706 Yang, J., F. Ding, R. M. Ramirez, W. R. Peltier, Y. Hu, and Y. Liu, 2017: Abrupt climate transition
707 of icy worlds from snowball to moist or runaway greenhouse. *Nature Geoscience*, **10** (8), 556–
708 560, doi:10.1038/ngeo2994, URL <http://www.nature.com/doi/10.1038/ngeo2994>.

709 Yang, J., W. R. Peltier, and Y. Hu, 2012: The Initiation of Modern Soft Snowball and Hard
710 Snowball Climates in CCSM3. Part II: Climate Dynamic Feedbacks. *Journal of Climate*,
711 **25 (8)**, 2737–2754, doi:10.1175/JCLI-D-11-00190.1, URL [http://journals.ametsoc.org/doi/abs/
712 10.1175/JCLI-D-11-00190.1](http://journals.ametsoc.org/doi/abs/10.1175/JCLI-D-11-00190.1).

713 **LIST OF FIGURES**

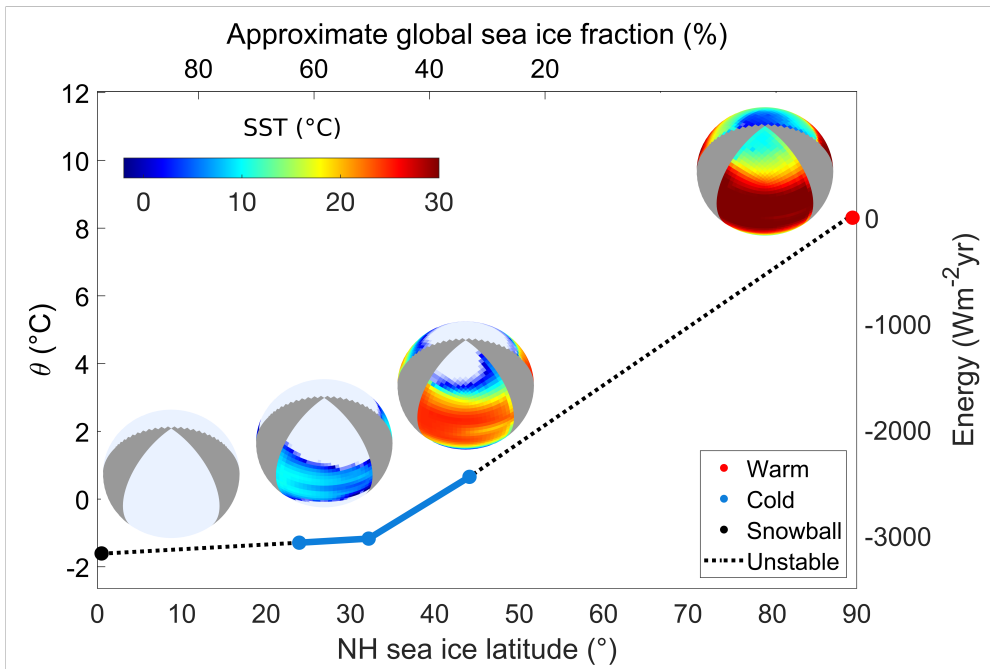
- 714 **Fig. 1.** A graphical representation of the 3 equilibria of our climate model: Warm, Cold and Snow-
715 ball. On the x-axis, we plot the latitude of NH sea ice extent (bottom axis) and ice fraction
716 (top axis). On the y-axis, we plot the ocean-mean potential temperature, θ , (left axis) and
717 energy level (right axis). The thermal energy stored in the ocean dominates over all other
718 sources. The unstable (dotted) lines are linear interpolations between the stable states found
719 in the model. In these ranges of sea ice latitudes and θ , no stable solution can be found. The
720 globes show the SST and sea ice extent of the Warm reference, Cold reference, Waterbelt
721 and Snowball states (from right to left). 39
- 722 **Fig. 2.** Zonally-averaged ocean potential temperature (color shading) for the Warm reference, Cold
723 reference, Waterbelt and Snowball states expressed on a stretched depth scale to highlight
724 the thermal structure of the upper ocean. The annual-mean sea ice cover in each hemisphere
725 is denoted by the thick black lines. The zonally-averaged ocean overturning streamfunction
726 (in Sv) is shown with clockwise circulation represented by solid lines and anticlockwise cir-
727 culation by dotted lines, with a contour interval of 10 Sv. The zonally-averaged meridional
728 ocean heat transport (in PW) is shown above each panel. Note the different scales of OHT. . . . 40
- 729 **Fig. 3.** (left) Bifurcation diagram of the climate model expressed in terms of the NH sea ice latitude
730 (left axis) versus the forcing F (bottom axis). F is calculated relative to the reference solar
731 constant $S_0 = 341.5 \text{ Wm}^{-2}$. The right axis indicates the approximate global mean SST and
732 the top axis shows the solar constant. The thick lines show the range of stable Warm (red),
733 Cold (blue) and Snowball (black) states. The black dotted lines indicate unstable NH sea
734 ice latitudes. Each red circle, blue square, green triangle and black diamond shows the
735 equilibrated state of a simulation started from the Warm (W), Cold (C), Waterbelt (WB) and
736 Snowball (S) states, respectively. (right) Schematic plot (not to scale) representing the stable
737 (solid) and unstable (dotted) branches of the bifurcation diagram. The red arrows outline a
738 possible path along the diagram starting from a Warm state and the blue arrows shows a
739 different path starting from a Cold state. $F_{w/c}$ and $F_{c/s}$ are transition thresholds between the
740 Warm/Cold and the Cold/Snowball equilibria respectively. F_{wb} ($= -5 \text{ Wm}^{-2}$) is the forcing
741 below which the Cold states become Waterbelt-like. 41
- 742 **Fig. 4.** Transition times to reach either the Waterbelt (circles) or Snowball (squares) climate for step
743 simulations starting from the Warm reference state (red) and Cold reference state (blue).
744 The Snowball transition times obtained by VM2010 are also plotted (in orange squares)
745 and scaled by a factor $f_{vm} = 1.5$ for ease of comparison with simulations starting from the
746 Warm reference state. Solid lines are corresponding estimates from the 1-box model with
747 the following parameter values: for a Warm start, $\lambda_w = 0.72 \text{ Wm}^{-2}$ and $H = 2416 \text{ m}$ (red
748 line); for a Cold start, $\lambda_c = 0.95 \text{ Wm}^{-2}$ and $H = 1149 \text{ m}$ (blue line); for VM2010, $\lambda_{vm} = 3.3$
749 Wm^{-2} , $H = 2603 \text{ m}$ and $f_{vm} = 1.5$ (orange line). 42
- 750 **Fig. 5.** Time evolution of the whole-ocean mean potential temperature anomaly following 1-year
751 long eruptions in our coupled model for a range of forcing magnitudes and starting states.
752 (left) Absolute temperature anomaly response, where the shading represents the 2σ range of
753 unforced variability in the control run. (right) Normalized responses with respect to the peak
754 cooling, which in each case occurs at the end of the first year, the time at which the forcing
755 is turned off. Solid lines are simulation results from the climate model, whereas dotted lines
756 are exponential fits to the following simulations: $F = -105 \text{ Wm}^{-2}$ run from Warm (red), $F =$
757 -89 Wm^{-2} from Cold (blue) and $F = -108 \text{ Wm}^{-2}$ from Very Warm (pink). 43
- 758 **Fig. 6.** Global-mean ocean potential temperature anomaly, plotted as a function of depth, follow-
759 ing impulse cooling forcings lasting 1 year, with a 50-year time averaging window. The

760 shading represents the 2σ level of unforced variability estimated from the relevant control
 761 simulation. The panels present results from the following simulations: (a) $F = -105 \text{ Wm}^{-2}$
 762 starting from Warm, (b) $F = -35 \text{ Wm}^{-2}$ starting from Warm, (c) $F = +31 \text{ Wm}^{-2}$ starting from
 763 Warm, and (d) $F = -108 \text{ Wm}^{-2}$ starting from Very Warm. The dotted lines in panel (a) show
 764 temperature profiles obtained from a 1D diffusive model with a diffusivity $\kappa = 3 \times 10^{-5}$
 765 m^2s^{-1} 44

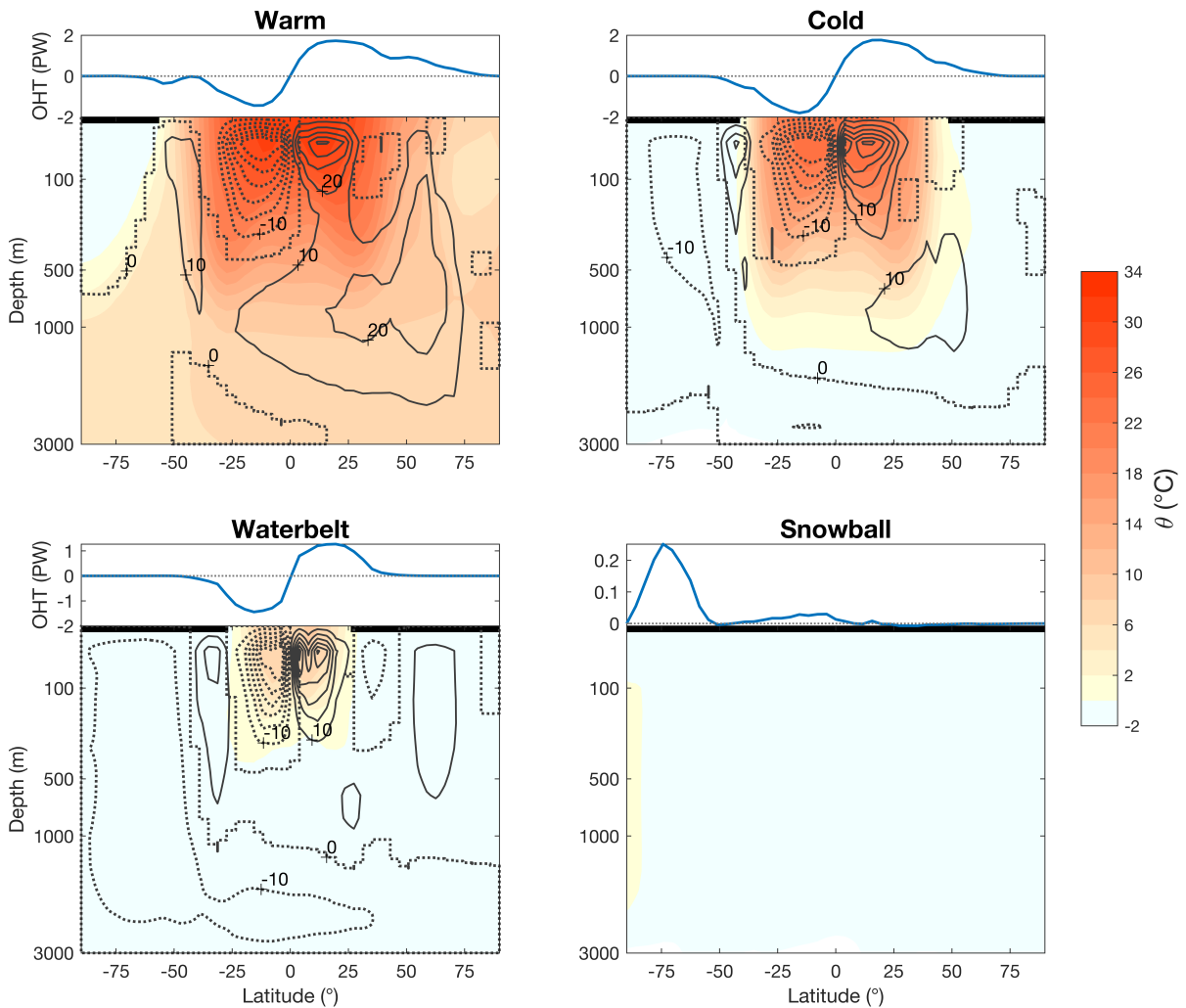
766 **Fig. 7.** (left) The response of global-mean ocean temperature, θ , to repeated 1-year eruptions every
 767 $\tau_i = 10$ years beginning from a Warm start with $F = -105 \text{ Wm}^{-2}$ (red) and a Cold start with
 768 $F = -89 \text{ Wm}^{-2}$ (dark blue). Step simulation responses are also shown for a Warm start with
 769 $F = -11 \text{ Wm}^{-2}$ (orange) and for a Cold start with $F = -9 \text{ Wm}^{-2}$ (light blue). Box model step
 770 responses for a Warm start with $F = -11 \text{ Wm}^{-2}$ (black dotted) and for a Cold start with $F =$
 771 -9 Wm^{-2} (green dotted). (right) Sea ice fraction response in the climate model simulations. . . . 45

772 **Fig. 8.** Estimates of state transition times for forcings consisting of repeated volcanic eruptions
 773 lasting 1 year, every τ_i years. The transition times are estimated using the step response
 774 under an average forcing F_{av} , for a range of forcing magnitudes F and eruption intervals
 775 τ_i . The points below the white dotted line are transitions to a Snowball. Points between
 776 the white and red dotted lines are transitions to the Waterbelt climate. Points between the
 777 red and black dotted lines are transitions to Cold. The straight contours represent constant
 778 values of F_{av} . Panel (a) and (b) show transition times when starting from the Cold and Warm
 779 reference climates, respectively. Note the different scales for the two panels. 46

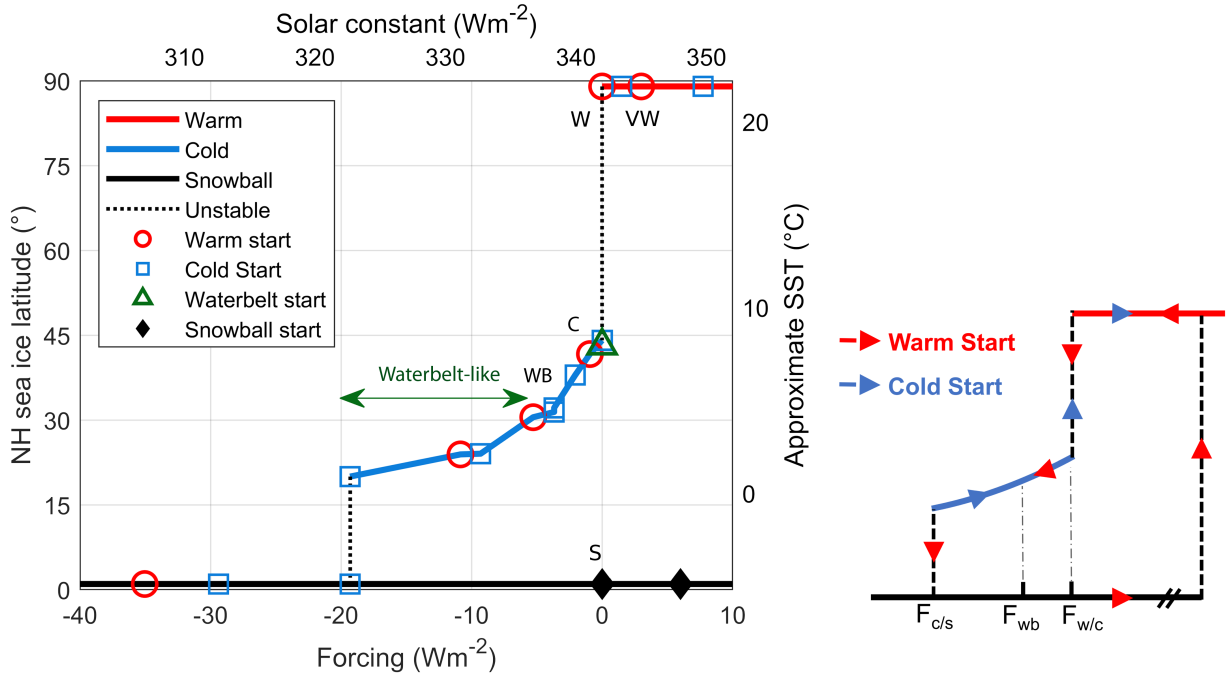
780 **Fig. A1.** Bifurcation diagrams obtained from the EBM for a range of δ values. All other parameters
 781 are fixed to: $A = 210 \text{ Wm}^{-2}$, $B = 1.5 \text{ Wm}^{-2}\text{K}^{-1}$, $a_0 = 0.7$, $a_i = 0.4$, $s_2 = -0.48$, $h_{min} =$
 782 0.67m , $k_i = 2 \text{ Wm}^{-2}\text{K}^{-1}$, $T_f = 0 \text{ }^\circ\text{C}$, $\Psi = 4 \text{ PW}$ and $N = 4$. Solid curves are obtained from
 783 the analytical model, whereas the dotted lines are results from the numerical solution of the
 784 EBM, which only picks out the stable branches of the diagram. 47



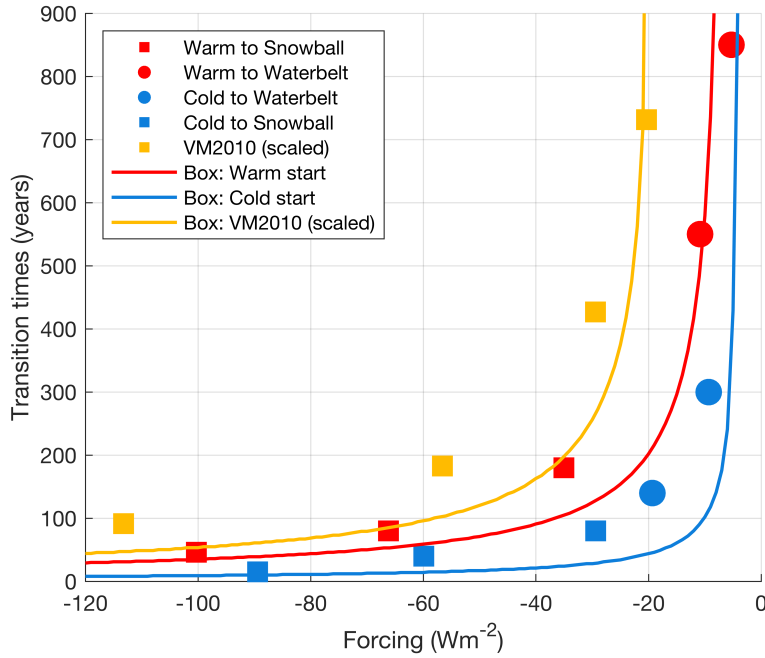
785 FIG. 1. A graphical representation of the 3 equilibria of our climate model: Warm, Cold and Snowball. On
 786 the x-axis, we plot the latitude of NH sea ice extent (bottom axis) and ice fraction (top axis). On the y-axis, we
 787 plot the ocean-mean potential temperature, θ , (left axis) and energy level (right axis). The thermal energy stored
 788 in the ocean dominates over all other sources. The unstable (dotted) lines are linear interpolations between the
 789 stable states found in the model. In these ranges of sea ice latitudes and θ , no stable solution can be found. The
 790 globes show the SST and sea ice extent of the Warm reference, Cold reference, Waterbelt and Snowball states
 791 (from right to left).



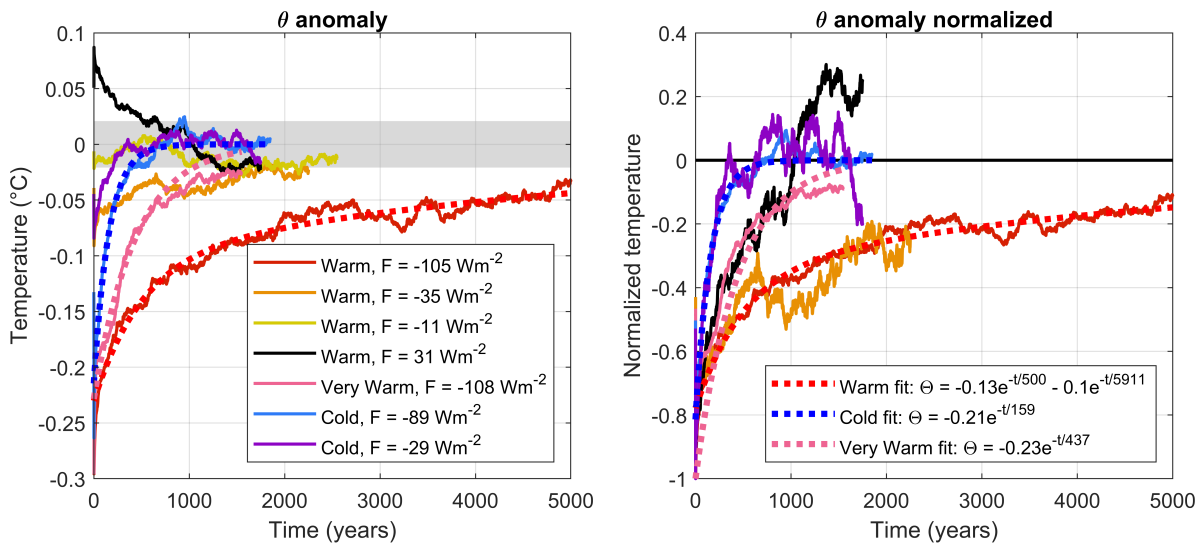
792 FIG. 2. Zonally-averaged ocean potential temperature (color shading) for the Warm reference, Cold reference,
 793 Waterbelt and Snowball states expressed on a stretched depth scale to highlight the thermal structure of the
 794 upper ocean. The annual-mean sea ice cover in each hemisphere is denoted by the thick black lines. The
 795 zonally-averaged ocean overturning streamfunction (in Sv) is shown with clockwise circulation represented by
 796 solid lines and anticlockwise circulation by dotted lines, with a contour interval of 10 Sv. The zonally-averaged
 797 meridional ocean heat transport (in PW) is shown above each panel. Note the different scales of OHT.



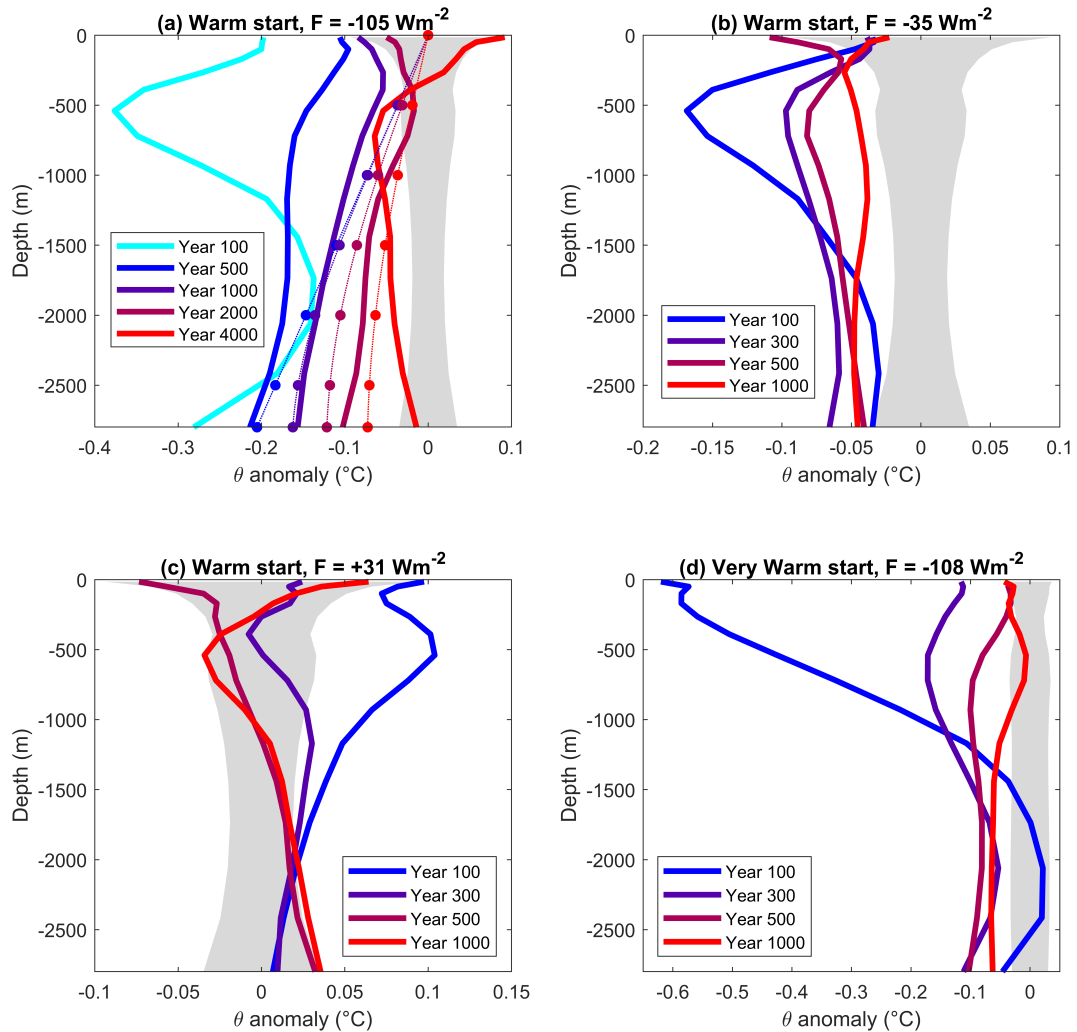
798 FIG. 3. (left) Bifurcation diagram of the climate model expressed in terms of the NH sea ice latitude (left
 799 axis) versus the forcing F (bottom axis). F is calculated relative to the reference solar constant $S_0 = 341.5$
 800 Wm^{-2} . The right axis indicates the approximate global mean SST and the top axis shows the solar constant. The
 801 thick lines show the range of stable Warm (red), Cold (blue) and Snowball (black) states. The black dotted lines
 802 indicate unstable NH sea ice latitudes. Each red circle, blue square, green triangle and black diamond shows the
 803 equilibrated state of a simulation started from the Warm (W), Cold (C), Waterbelt (WB) and Snowball (S) states,
 804 respectively. (right) Schematic plot (not to scale) representing the stable (solid) and unstable (dotted) branches
 805 of the bifurcation diagram. The red arrows outline a possible path along the diagram starting from a Warm state
 806 and the blue arrows shows a different path starting from a Cold state. $F_{w/c}$ and $F_{c/s}$ are transition thresholds
 807 between the Warm/Cold and the Cold/Snowball equilibria respectively. F_{wb} ($= -5 Wm^{-2}$) is the forcing below
 808 which the Cold states become Waterbelt-like.



809 FIG. 4. Transition times to reach either the Waterbelt (circles) or Snowball (squares) climate for step simula-
 810 tions starting from the Warm reference state (red) and Cold reference state (blue). The Snowball transition times
 811 obtained by VM2010 are also plotted (in orange squares) and scaled by a factor $f_{vm} = 1.5$ for ease of comparison
 812 with simulations starting from the Warm reference state. Solid lines are corresponding estimates from the 1-box
 813 model with the following parameter values: for a Warm start, $\lambda_w = 0.72 Wm^{-2}$ and $H = 2416$ m (red line); for a
 814 Cold start, $\lambda_c = 0.95 Wm^{-2}$ and $H = 1149$ m (blue line); for VM2010, $\lambda_{vm} = 3.3 Wm^{-2}$, $H = 2603$ m and $f_{vm} =$
 815 1.5 (orange line).

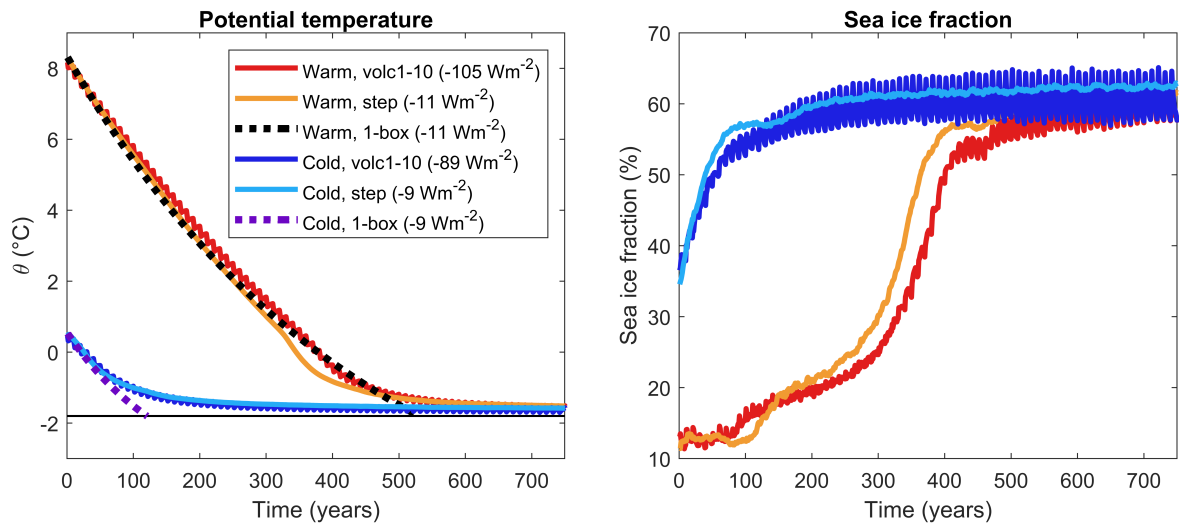


816 FIG. 5. Time evolution of the whole-ocean mean potential temperature anomaly following 1-year long erup-
 817 tions in our coupled model for a range of forcing magnitudes and starting states. (left) Absolute temperature
 818 anomaly response, where the shading represents the 2σ range of unforced variability in the control run. (right)
 819 Normalized responses with respect to the peak cooling, which in each case occurs at the end of the first year, the
 820 time at which the forcing is turned off. Solid lines are simulation results from the climate model, whereas dotted
 821 lines are exponential fits to the following simulations: $F = -105 \text{ Wm}^{-2}$ run from Warm (red), $F = -89 \text{ Wm}^{-2}$
 822 from Cold (blue) and $F = -108 \text{ Wm}^{-2}$ from Very Warm (pink).

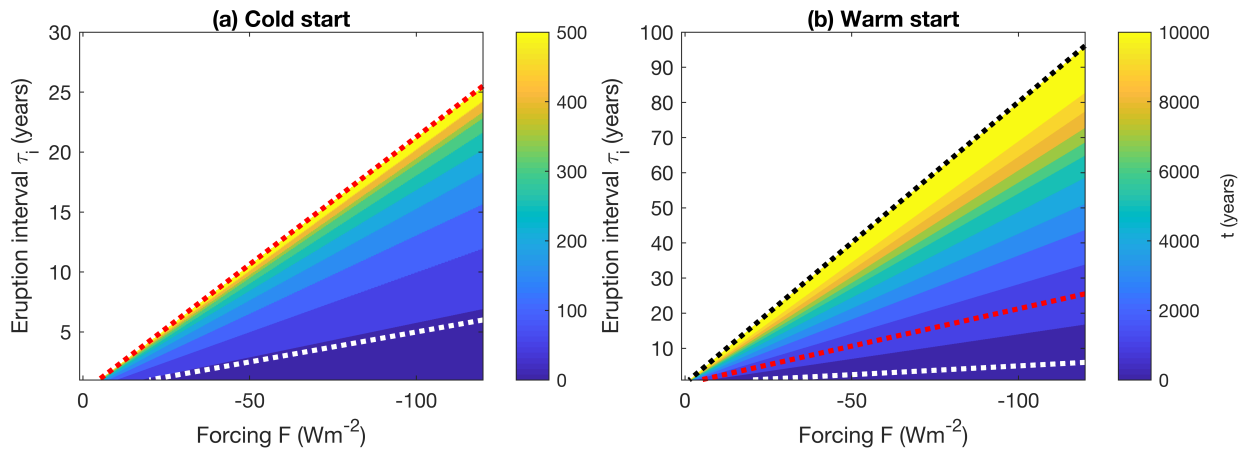


823 FIG. 6. Global-mean ocean potential temperature anomaly, plotted as a function of depth, following impulse
 824 cooling forcings lasting 1 year, with a 50-year time averaging window. The shading represents the 2σ level
 825 of unforced variability estimated from the relevant control simulation. The panels present results from the
 826 following simulations: (a) $F = -105 \text{ Wm}^{-2}$ starting from Warm, (b) $F = -35 \text{ Wm}^{-2}$ starting from Warm, (c) $F =$
 827 $+31 \text{ Wm}^{-2}$ starting from Warm, and (d) $F = -108 \text{ Wm}^{-2}$ starting from Very Warm. The dotted lines in panel (a)
 828 show temperature profiles obtained from a 1D diffusive model with a diffusivity $\kappa = 3 \times 10^{-5} \text{ m}^2 \text{ s}^{-1}$.

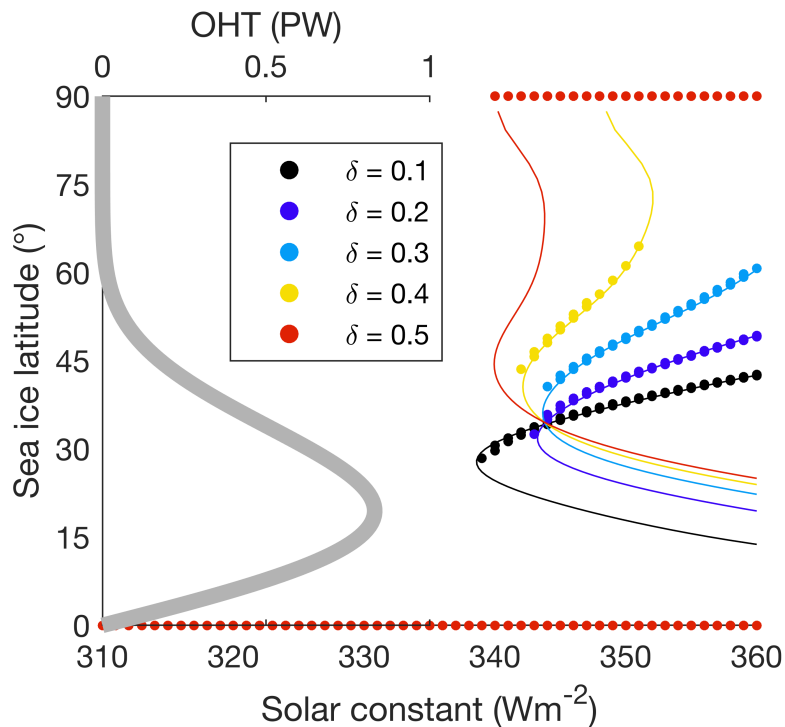
Repeated eruptions versus step forcing



829 FIG. 7. (left) The response of global-mean ocean temperature, θ , to repeated 1-year eruptions every $\tau_i = 10$
 830 years beginning from a Warm start with $F = -105 \text{ Wm}^{-2}$ (red) and a Cold start with $F = -89 \text{ Wm}^{-2}$ (dark blue).
 831 Step simulation responses are also shown for a Warm start with $F = -11 \text{ Wm}^{-2}$ (orange) and for a Cold start with
 832 $F = -9 \text{ Wm}^{-2}$ (light blue). Box model step responses for a Warm start with $F = -11 \text{ Wm}^{-2}$ (black dotted) and for
 833 a Cold start with $F = -9 \text{ Wm}^{-2}$ (green dotted). (right) Sea ice fraction response in the climate model simulations.



834 FIG. 8. Estimates of state transition times for forcings consisting of repeated volcanic eruptions lasting 1 year,
 835 every τ_i years. The transition times are estimated using the step response under an average forcing F_{av} , for a
 836 range of forcing magnitudes F and eruption intervals τ_i . The points below the white dotted line are transitions to a
 837 Snowball. Points between the white and red dotted lines are transitions to the Waterbelt climate. Points between
 838 the red and black dotted lines are transitions to Cold. The straight contours represent constant values of F_{av} .
 839 Panel (a) and (b) show transition times when starting from the Cold and Warm reference climates, respectively.
 840 Note the different scales for the two panels.



841 Fig. A1. Bifurcation diagrams obtained from the EBM for a range of δ values. All other parameters are fixed
 842 to: $A = 210 Wm^{-2}$, $B = 1.5 Wm^{-2}K^{-1}$, $a_0 = 0.7$, $a_i = 0.4$, $s_2 = -0.48$, $h_{min} = 0.67m$, $k_i = 2 Wm^{-2}K^{-1}$, $T_f = 0^\circ C$,
 843 $\Psi = 4 PW$ and $N = 4$. Solid curves are obtained from the analytical model, whereas the dotted lines are results
 844 from the numerical solution of the EBM, which only picks out the stable branches of the diagram.